

Radar Odometry with Recursive-RANSAC

ERIC B. QUIST
PETER C. NIEDFELDT
RANDAL W. BEARD
Brigham Young University
Provo, UT, USA

This paper explores the use of radar odometry for Global Positioning System-denied navigation. The range progression from arbitrary ground-based point scatterers is used to estimate an unmanned aerial vehicle's relative motion. In high clutter environments, the recursive-RANSAC algorithm provides robust and efficient feature identification, data association, and tracking. The tracked feature range measurements are integrated with inertial measurement unit measurements in an extended Kalman filter. Real flight data from a cluttered environment are used to validate the results.

Manuscript received November 7, 2014; revised June 21, 2015, December 1, 2015, December 30, 2015; released for publication April 12, 2016.

DOI. No. 10.1109/TAES.2016.140829.

Refereeing of this contribution was handled by Z. Zhu.

Authors' address: Brigham Young University, Electrical and Computer Engineering, 459 Clyde Building, Provo, UT 84602, USA.
Corresponding author is E. B. Quist, E-mail: (eric.quist@gmail.com).

0018-9251/16/\$26.00 © 2016 IEEE

I. INTRODUCTION

Unmanned aerial vehicle (UAV) navigation is predicated on the aircraft's ability to estimate its motion in both known and unknown environments. Modern unmanned systems typically use an inertial measurement unit (IMU) to estimate their motion and the Global Positioning System (GPS) to correct for IMU drift. As GPS is easily jammed or may not be available, it is essential to develop robust navigation algorithms that continue to operate properly, even when the GPS signal is lost.

A variety of sensors have been considered for GPS-denied navigation. Optical sensors are severely limited by weather and nighttime navigation. Additionally, their sensitivity and accuracy degrade at the long standoff ranges often experienced by aircraft [1–6]. Beacons provide accurate range but rely on cooperative, active transmitters that are distributed throughout the navigated environment [7–10]. Sonar measures range but is very poor at identifying and isolating environmental features [11–14]. In contrast, radar sensors provide accurate range, are robust to environmental conditions, and are excellent at identifying individual features [15–25]. Additionally the size, weight, and power (SWaP) footprint of many radars has been drastically reduced with recent technology advancements [26–29], thus allowing it to be an optional payload on small UAVs.

The use of radar for GPS-denied navigation relies on the radar's ability to identify, localize, and track ground point scatterers. Accordingly, existing navigation algorithms are directly dependent on each radar's specific mode of operation. Terrain-aided navigation [30–32] systems use a map containing known terrain variation in conjunction with a radar, acting as a range-sensing altimeter, for localization. Using multiple antennas, many radars are configured to measure both range and azimuth angle to ground point scatterers. In this configuration, some solutions navigate using an occupancy grid of point scatterers [33, 34], while a simultaneous localization and mapping [25, 35] approach iteratively creates, updates, and localizes a map of tracked features. Rather than use multiple antennas to measure the azimuth angle to scatterers, an alternative configuration uses a narrow-beam-width, rotating receive antenna [36, 37], similar to many light detection and ranging solutions [38–42]. While effective, the size and complexity of these systems is prohibitive for small UAVs. For these small systems, the use of a single, nonrotating, wide-beam-width antenna would minimize both the size and the weight of the radar payload.

A more simplistic system uses a radar configuration commonly used by synthetic aperture radars (SARs). These systems typically use a single, side-looking receive antenna to measure the range to features. When a coherent radar is used, range rate is also measured. In this configuration, Kaufman et al. [24] navigate using unknown ground-based point scatterers. Their approach identifies

possible features using an adaptive signal-to-noise ratio thresholding algorithm. A global nearest neighbor (GNN) scheme associates measurements from successive chirps, while a binomial M-out-of-N detector [43, 44] is used to distinguish the actual point-scatterer range progression from momentary noise. An extended Kalman filter (EKF) uses an IMU for state prediction, with the update provided by the range and Doppler measurements for tracked scatterers. Their simulations show promising results, though only two-dimensional navigation was simulated. Additionally, their simulations contain white, uniform clutter, while a real SAR's dense return would significantly deteriorate the accuracy of a GNN data association scheme. Recently, the algorithm was tested using a real radar in a controlled indoor environment using several ideal corner reflectors [23] and a tactical-grade IMU. Their results indicated a respectable 4.5% drift, though this is inconsistent with their air-based simulations, which report a 0.01% drift with a commercial-grade IMU and 0.0083% drift with a tactical-grade IMU [24].

In previous work, we present an alternative approach that uses only range measurements from an airborne SAR [45] while also using the same radar as an altimeter [46]. This approach uses an image-processing prefilter in conjunction with a Hough transform to identify point scatterers from a range-compressed image. Once identified, a greedy algorithm identifies pairs of scatterers that are used to triangulate both the point scatterer's positions and the aircraft's motion. The resulting measurements are used in conjunction with an IMU in an EKF to estimate the aircraft's motion. Real flight results are explored while also assessing the accuracy of the algorithm while the aircraft is banking [46]. While these results are the first to present real flight results, though, the greedy nature of their algorithm and their heading assumptions result in an algorithm that is not robust to dynamic flight environments.

In previous work, we implement the newly developed recursive random sample consensus (R-RANSAC) algorithm [47, 48] to estimate the location of point scatterers with respect to an aircraft using range-only measurements [49]. R-RANSAC relies on the traditional random sample consensus (RANSAC) algorithm, which is a batch algorithm for estimating the parameters of a single signal in clutter and has found wide use within the computer vision community due to its simplicity and robustness. The premise of the standard RANSAC algorithm is to randomly select minimum subsets from a batch of data to form numerous hypotheses of an underlying signal, where the hypothesis with the most supporting measurements, or consensus set, is identified as the most accurate hypothesis [50].

The R-RANSAC algorithm extends the standard RANSAC algorithm in two notable ways. First, it stores multiple hypotheses between time steps and recursively estimates their parameters using sequential measurements, for example, using the recursive least-squares filter; measurements whose residual is within a threshold to the

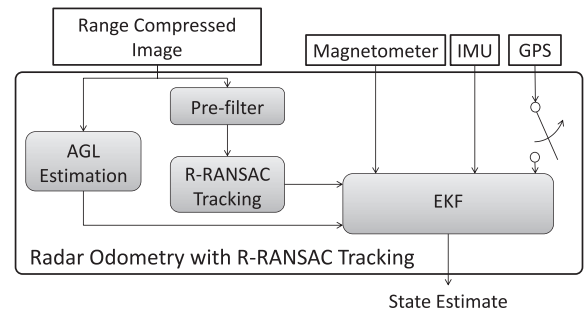


Fig. 1. Radar odometry block diagram.

stored hypotheses are identified as inliers and used to update existing hypotheses, while outliers are used to seed a new RANSAC hypothesis. The second extension is a natural consequence of storing multiple hypotheses between time steps in that R-RANSAC is able to estimate the parameters of multiple signals simultaneously; hypotheses that have a consensus set above a threshold are identified as valid hypotheses. In [49], we found that using R-RANSAC drastically decreases the computational complexity compared to the Hough transform used in [45, 46]. Additionally, the R-RANSAC algorithm is robust in cluttered environments [48], which is a known shortcoming of the GNN approach [51].

This paper presents a novel, robust, scatterer-tracking and navigation algorithm while demonstrating its results with real flight radar data. This paper is novel in several ways. First, this paper uses the newly developed R-RANSAC algorithm to perform data association, as is explored in [49]. Second, this paper removes the constant-heading assumption in [46], thus providing significant robustness to dynamic flight tracks. Third, rather than tracking scatterers using a Cartesian coordinate system, as in [24], this paper uses a two-dimensional, polar coordinate system, which is more appropriate given the azimuth uncertainty [52]. Further, this paper assumes the radar is not coherent, and as such the radar measures only the range to ground point scatterers. Finally, the results in this paper show a reduced drift rate using a navigation-grade IMU and real flight data.

The paper is organized as follows. Section II describes the use of R-RANSAC for scatterer identification and tracking, while section III describes the system's state-space model and the associated EKF. Section IV presents the simulated and real radar results.

II. RADAR ODOMETRY WITH R-RANSAC

The proposed tracking radar odometry algorithm is outlined in Fig. 1. A range-compressed image is the input to the algorithm. The image is initially prefiltered and used to generate an above-ground level (AGL) estimate. R-RANSAC identifies, tracks, and measures the range to scatterers in the prefiltered image. An EKF uses the IMU to propagate the system state. The EKF uses the range measurement, the AGL estimate, GPS (when available),

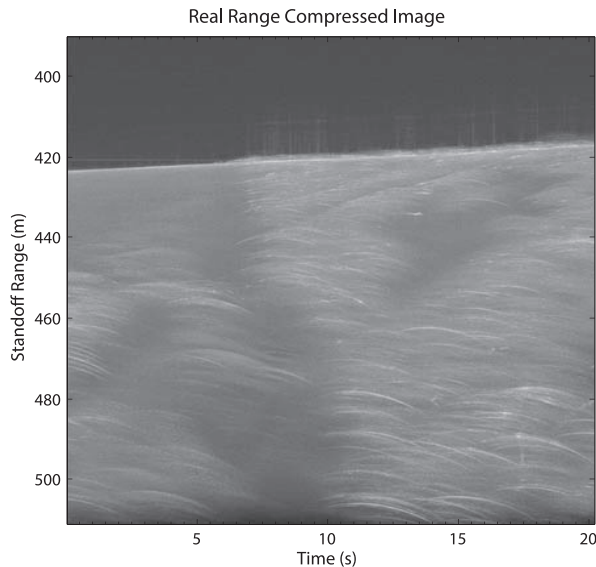


Fig. 2. Range-compressed image from a real flight. The bright hyperbolas in the image are due to the range progression of strong point scatterers. The dark portion at the top of the image indicates no objects reflecting at that range. At nadir, the return power drastically increases as ground scatterers reflect the radar signal back to the aircraft.

and the magnetometer to update the aircraft's and scatterers' states, correcting drift inherent in the IMU.

A. AGL Measurement

The AGL measurement uses the radar as an altimeter. As can be seen in the range-compressed image shown in Fig. 2, the upper portion of the image is relatively dark, indicating no radar return. As the range increases, nadir is measured as the range at which there is a large increase in return power as the radar signal reflects off of nadir (see [46] for more detail).

B. Resolving Strong Point Scatterers

Performing motion estimation with radar requires accurate detecting, associating, and tracking of point scatterers. When navigating an environment with very little radar return power, such as over a large body of water, strong point scatterers are easily detected and tracked. In contrast, when navigating unknown environments containing clutter, noise sources, and a large number of strong and weak point scatterers, the detection and tracking become significantly more difficult. The difficulty is amplified when using arbitrary point scatterers for navigation, as the difference between a "good" and a "bad" point scatterer may be determined by the scatterer's radar reflectivity, its motion, or even the reflectivity of interfering neighboring scatterers. Additionally, any error in detection, tracking, or association directly affects the motion estimation errors.

1) Image Prefiltering for Scatter Detection:

Range-compressed imagery has significant amounts of noise, as can be seen in Fig. 2. Typically, a thresholding

scheme is used to identify scatterers from noise. We also use a thresholding scheme; however, some initial preprocessing is used to help remove the noise prior to identifying scatterers. First, a weighted local pixel average is removed from the image. Second, the image is smoothed, followed by a decimation step, thus reducing the processing requirements of the system. Further processing involves removing a weighted, range-dependent mean. Finally, a threshold is applied, resulting in a binary image indicating possible scatterers (see [46] for a more thorough description).

2) *Data Association and Filtering:* The process of tracking point scatterers between time steps is an instance of the general multiple target tracking (MTT) problem, where both the number and the individual state vectors of multiple signals are recursively estimated. Developing a robust MTT algorithm has been an active field of research since at least the 1960s. Since that time, numerous MTT algorithms have been developed, including GNN [53], joint probabilistic data association (JPDA) [54], multiple hypothesis tracking (MHT) [55, 56], and probability hypothesis density (PHD) [57, 58] filters.

Nearest neighbor algorithms, such as the GNN filter, associate the statistically nearest measurements to existing tracks. While computationally efficient, GNN has no mechanism to manage the initiation and deletion of new trackable objects. In their work, Kauffman et al. [20] use a binary M-out-of-N detector to identify persistent scatterers and the GNN algorithm to filter new measurements to estimate the scatter positions. Unfortunately, the GNN state estimates can diverge in cluttered environments [51].

For this reason, our previous work used the Hough transform [45] to identify scatterers in the range-compressed image. While functional, the Hough transform is a batch algorithm and is very processing intensive. Additionally, the Hough transform is a voting algorithm with a finite set of possible coefficients; in [45], further processing is necessary to identify and track strong scatterers.

All the other MTT algorithms mentioned above suffer from at least one critical drawback: the JPDA filter does not have a track management algorithm, the MHT is computationally complex and difficult to implement, and the PHD filter has poor track continuity in highly cluttered environments. Instead, we use the newly developed R-RANSAC algorithm, which has been shown to build on RANSAC's robustness while handling multiple coefficient sets and sequential measurements [47, 48]. A review of the R-RANSAC algorithm is provided in the following section.

3) *The R-RANSAC Algorithm:* The R-RANSAC algorithm was originally developed in [47] to estimate the parameters of static signals. In [49], we apply R-RANSAC to estimate the location of point scatterers relative to an aircraft using range-compressed images. We show R-RANSAC to be as accurate as the Hough transform while decreasing the processing time significantly. In this section, we review our original implementation of

R-RANSAC to track point scatterers to provide context for later improvements in the current iteration of our work.

At each time step, or chirp in a radar application, a set of measurements is received denoting the ranges to point scatterers or clutter. Rather than performing the standard RANSAC algorithm after each new chirp, R-RANSAC stores multiple scatterer hypotheses and identifies each new measurement as an outlier or inlier to existing hypotheses. Each outlier is used to seed the standard RANSAC algorithm to generate a new hypothesis from past data to describe the measurement. Inliers are used to update the parameters and consensus set of existing hypotheses [49].

The R-RANSAC algorithm is a modular framework that can incorporate various underlying data fusion techniques [48]. For example, after identifying the set of outliers, a measurement weighting can be assigned to each inlier measurement for use during the update step. In [49], we use an all neighbor's approach, where all inlier measurements are averaged together into a single pseudomeasurement. Alternatively, other measurement weighting techniques, such as nearest neighbor or probabilistic data association (PDA) [59], can be used.

4) *Tracking*: Our previous algorithms used the Hough transform and R-RANSAC exclusively for data association. Tracking the range progression of the point scatterers involved an all-neighbors approach to detect deviations from the hyperbolic track. In this paper, we use the R-RANSAC algorithm for both data association and feature tracking. Rather than rely on ideal, hyperbolic range progression curves, we model the range progressions using polynomials. To support dynamic flight paths, a short time window is selected so that within the small window, the range curve resembles a second-order polynomial.

While the R-RANSAC algorithm is used for both data association and feature tracking, our navigational requirements demand that the aircraft and features coexist in the state-space model. Accordingly, the data association and tracking performed by R-RANSAC are used to provide the EKF with feature measurements. Additionally, R-RANSAC's tracking is used to flag the EKF to create new scatterers and prune stagnant scatterers from the state-space model.

C. Implementing R-RANSAC for Data Association and Tracking

Accurate navigation using point scatterers is particularly reliant on accurate detection, association, and tracking. When accurate association and tracking is properly performed, as shown in Fig. 3, accurate navigation is possible. Any error that exists is properly identified as the radar's range measurement error or motion error of the aircraft.

In contrast, when association and tracking errors do occur, the error is improperly construed to be a range

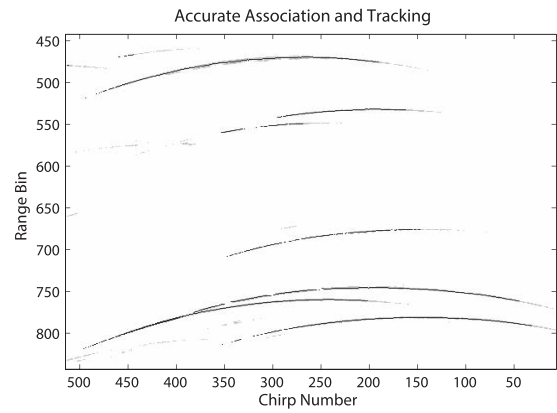


Fig. 3. Accurate association and tracking for real range compressed image. The real range compressed image is shown in gray, while the identified and tracked features are shown in black.

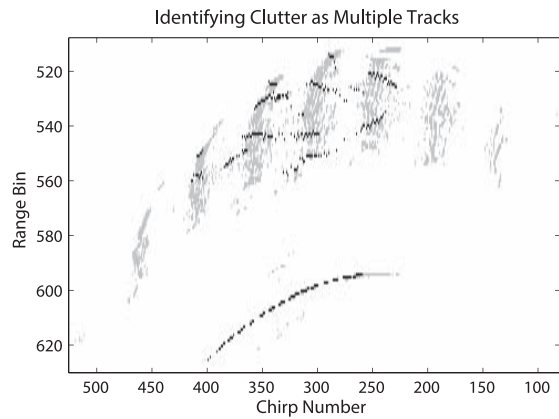
measurement error or an aircraft motion error. Consider a few possible error scenarios:

- Clutter is improperly identified as multiple point scatterers, as shown in Fig. 4a. While the lower feature was properly identified and tracked, the upper clutter is mistaken for multiple features. The tracked range progression of each feature is widely diverging.
- Range progression drift results in improper feature association, as shown in Fig. 4b. Not only does the track drift result in switching tracked features, but a new feature is created to track the original feature.
- Feature proximity (in range) results in improper feature measurements, as shown in Fig. 4c. The range return from the lower three tracks is improperly identified as a measurement of the upper right track. As a result, proper identification of the bottom track is delayed.
- The tracking of features may prematurely end, as shown in the bottom track in Fig. 4c. While feature proximity resulted in a delayed identification, a combination of noise and nearby features results in the feature track being prematurely killed.

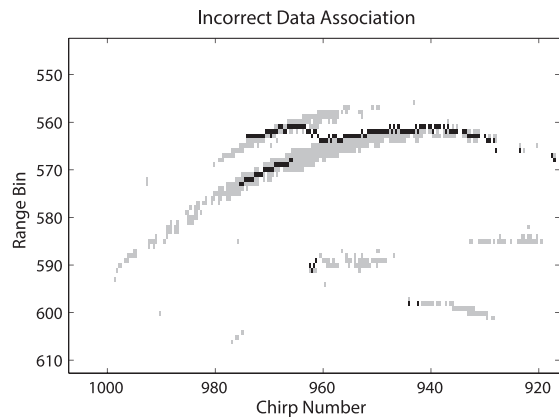
Proper tracking involves carefully balancing a variety of requirements. While short time windows allow for dynamic flight paths, they also increase the probability of unknowingly switching from one tracked scatterer to another. A high threshold allows for only features with a large number of measurements to be tracked but also delays the identification of tracks, thus resulting in a decreased number of measurements. These are particularly difficult, as the aircraft's antenna beam width limits the length of time that a scatterer is measurable.

To account for these requirements and limitations, a variety of modifications to the basic R-RANSAC framework were incorporated:

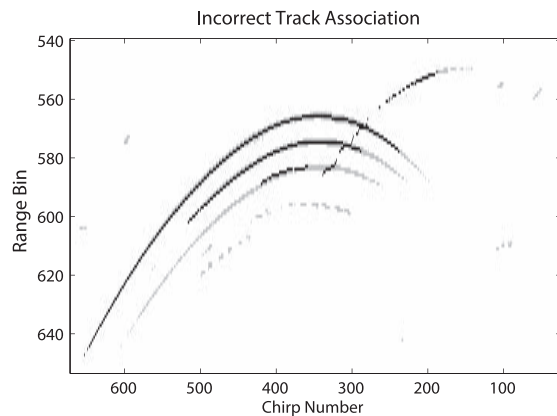
- When a new outlier is identified, rather than use RANSAC over all data points, it is used over a smaller window in range and time, surrounding the outlier under consideration. If a feature has sufficient neighboring



(a)



(b)



(c)

Fig. 4. Errors associated with incorrectly distinguishing clutter and features (a), track drift (b), and feature identification (c). All show a real range compressed image in gray, while the identified and tracked features are shown in black.

outliers, the entire R-RANSAC window is used to identify all inliers.

- If a long period of time or a large distance in range is separated consecutive inliers, the old samples were discarded and were considered as outliers.
- A constraint on the possible coefficient set was used to remove tracks that would be impossible given the aircraft's dynamics.

- RANSAC is intermittently instantiated on new outliers, thus decreasing the processing requirements.

- Two inlier thresholds were used in the R-RANSAC algorithm. One threshold is used to identify initial tracks, while the second is a higher threshold that identifies tracks with a sufficiently large inlier set to justify tracking in the EKF. While the first set of tracks is discarded whenever a better track is found, the second set is discarded only when it is stagnant or has fallen below its higher threshold.

- Many features have a very fine range return, while others smear across multiple range bins. Accordingly, rather than use the total number of inliers to determine support, the number of time samples with an inlier is used to identify good tracks.

- A PDA data association scheme, with a Mahalanobis distance, is used to weight new measurements.

D. Tracking Results

It is difficult to systematically assess the accuracy of the tracking solution using real data containing unknown point scatterers. While not ideal, using simulated data allows for accuracy of the tracking scheme to be assessed. A Monte Carlo simulation was performed using strong point scatterers. Fig. 5a shows the simulated average tracking error for each identified feature. Only identified and tracked errors are measured. As can be seen, the average error was .35 m, barely more than the .3 m pixel resolution. Fig. 5b indicates the number of range-compressed chirps where the point scatter was in the imagery but not identified as a track. The average of 30 chirps is expected, given the clutter in real imagery and the delay required to identify new features.

III. EKF AND THE APPLIED STATE-SPACE MODEL

This section describes our EKF, shown in Fig. 1. An indirect Kalman filter approach would have allowed computational savings, we have selected the more simplistic direct approach. Analysis indicates that either approach would result in comparable results [60–63]. The measurements are the IMU, a digital compass, the AGL estimate, and the range to each feature, as computed using the method described in the previous section. The output of the EKF are the aircraft position, velocity, and attitude estimates.

We assume the system model

$$\begin{aligned}\dot{\mathbf{x}} &= \mathbf{f}(\mathbf{x}, \mathbf{u} + \boldsymbol{\mu}) + \boldsymbol{\xi} \\ \dot{\mathbf{y}}_k &= \mathbf{h}(\mathbf{x}_k) + \nu_k,\end{aligned}$$

where $\boldsymbol{\xi}$ is the zero mean Gaussian system noise with covariance \mathbf{Q} , ν_k is the zero mean Gaussian measurement noise with covariance R , and \mathbf{y}_k indicates the discrete system measurements at time k .

In this paper, a continuous dynamics, discrete measurement, EKF [64], is used, as listed below.

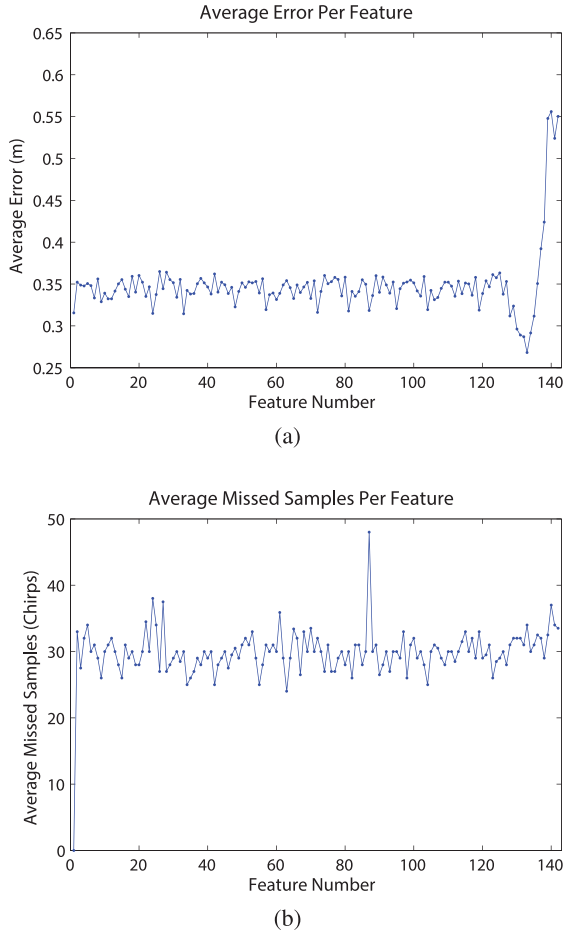


Fig. 5. Simulated error between truth and tracked measurements (a) and the number of simulated chirps where the feature was not tracked (b). The change in average errors of features 120–140 is due to their limited observation time.

Prediction Step:

$$\begin{aligned}\dot{\hat{\mathbf{x}}} &= f(\hat{\mathbf{x}}, \mathbf{u}) \\ \dot{\mathbf{P}} &= \frac{\partial f}{\partial \mathbf{x}} \mathbf{P} + \mathbf{P} \frac{\partial f^T}{\partial \mathbf{x}} + \mathbf{Q} + \frac{\partial f}{\partial \mathbf{u}} \mathbf{M} \frac{\partial f^T}{\partial \mathbf{u}}\end{aligned}$$

Measurement Step:

$$\begin{aligned}\mathbf{L} &= \mathbf{P}^- \frac{\partial h}{\partial \mathbf{x}} \left(\mathbf{R} + \frac{\partial h}{\partial \mathbf{x}} \mathbf{P}^- \frac{\partial h^T}{\partial \mathbf{x}} \right)^{-1} \\ \mathbf{P}^+ &= \left(\mathbf{I} - \frac{\partial h}{\partial \mathbf{x}} \right) \mathbf{P}^- \\ \hat{\mathbf{x}}^+ &= \hat{\mathbf{x}}^- + \mathbf{L} (\mathbf{y}_k - h(\hat{\mathbf{x}}^-)),\end{aligned}$$

where $\hat{\mathbf{x}}^-$ and \mathbf{P}^- denote $\hat{\mathbf{x}}$ and \mathbf{P} after the prediction step but before the measurement update and $\hat{\mathbf{x}}^+$ and \mathbf{P}^+ denote $\hat{\mathbf{x}}$ and \mathbf{P} after the measurement update. This section is organized as follows. First, the system state is described. The system state consists of both the aircraft and the scatterer states. Second, the state prediction model is described. Third, the update model for each sensor is

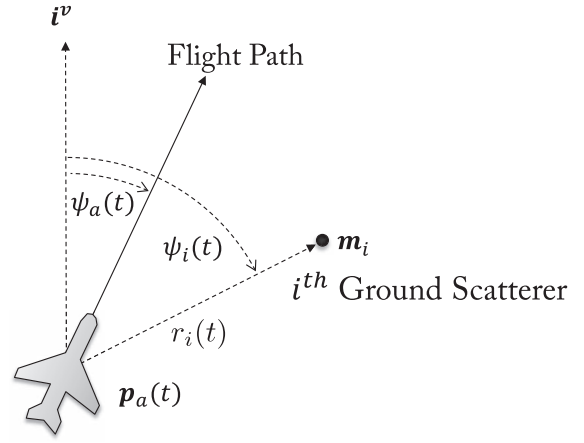


Fig. 6. Azimuth angle and range relative to the aircraft's vehicle frame.

derived. The final section discusses new scatterer initialization.

A. System State

The system state is

$$\mathbf{x} = [\mathbf{x}_a^T \quad \mathbf{x}_s^T]^T, \quad (1)$$

where \mathbf{x}_a is the aircraft state and \mathbf{x}_s represents the states of the n tracked scatterers, given as

$$\mathbf{x}_s = [\mathbf{x}_1^T \quad \dots \quad \mathbf{x}_n^T]^T.$$

1) *Aircraft State*: The aircraft state is represented as

$$\mathbf{x}_a = [\mathbf{p}_a^T \quad \dot{\mathbf{p}}_a^T \quad \boldsymbol{\Theta}_a^T]^T,$$

where the position of the aircraft is

$$\mathbf{p}_a = [n_a \quad e_a \quad h_a]^T,$$

where n_a is the North position, e_a is the East position, and h_a is the altitude and where the attitude is given by

$$\boldsymbol{\Theta}_a = [\phi_a \quad \theta_a \quad \psi_a]^T,$$

where ϕ_a , θ_a , and ψ_a represent the roll, pitch, and yaw, respectively [65].

2) *Point Scatterer State*: The ground point scatterer state is represented as

$$\mathbf{x}_i = \begin{bmatrix} r_i^g \\ \psi_i \end{bmatrix} = \begin{bmatrix} \sqrt{(n_i - n_a)^2 + (e_i - e_a)^2} \\ \text{atan} \left(\frac{e_i - e_a}{n_i - n_a} \right) \end{bmatrix},$$

where n_i and e_i are the North and East coordinates of the scatterer, r_i^g is the ground range to the scatterer, and ψ_i is the azimuth angle represented in the aircraft's body frame, ψ_i , shown in Fig. 6. Assuming a flat Earth, the elevation angle is represented as

$$\phi_i = \text{asin} \left(\frac{d_i - d_a}{r_i} \right). \quad (2)$$

The state model allows for the inertial position of the scatterer to be calculated as

$$\mathbf{p}_i = \begin{bmatrix} n_i \\ e_i \\ d_i \end{bmatrix} = \begin{bmatrix} n_a \\ e_a \\ 0 \end{bmatrix} + \begin{bmatrix} r_i^g \cos \psi_i \\ r_i^g \sin \psi_i \\ 0 \end{bmatrix}. \quad (3)$$

B. EKF State Prediction Model

A gyro and accelerometer are used as the input for the prediction model

$$\mathbf{u} = \begin{bmatrix} \mathbf{a}^b{}^\top & \boldsymbol{\omega}^\top \end{bmatrix}^\top,$$

where \mathbf{a}^b are the accelerometer measurements, as measured in the body frame, and $\boldsymbol{\omega}$ are the angular body rates measured by the gyros.

The prediction model is expressed as

$$\dot{\mathbf{x}} = f(\mathbf{x}, \mathbf{u}) = \begin{bmatrix} f_a(\mathbf{x}, \mathbf{u}) \\ f_0(\mathbf{x}, \mathbf{u}) \\ \vdots \\ f_N(\mathbf{x}, \mathbf{u}) \end{bmatrix}, \quad (4)$$

for N scatterers. The aircraft dynamics are defined as

$$f_a(\mathbf{x}, \mathbf{u}) = \begin{bmatrix} \mathbf{v} \\ \mathbf{g}^i + R_i^b(\phi, \theta, \psi) \mathbf{a}^b \\ S(\Theta) \boldsymbol{\omega} \end{bmatrix},$$

where $\mathbf{g}^i = [0 \ 0 \ g]^\top$ is the gravity vector in the inertial frame,

$$S(\Theta) = \begin{bmatrix} 1 & \sin \phi \tan \theta & \cos \phi \tan \theta \\ 0 & \cos \phi & -\sin \phi \\ 0 & \frac{\sin \phi}{\cos \theta} & \frac{\cos \phi}{\cos \theta} \end{bmatrix},$$

and $R_i^b(\phi, \theta, \psi)$ is the transformation from the body frame to the inertial frame.

The scatterer state propagation model is

$$\begin{aligned} \dot{\mathbf{x}}_i &= \begin{bmatrix} \dot{r}_i^g \\ \dot{\psi}_i \end{bmatrix} \\ &= \begin{bmatrix} -\dot{n}_a \cos \psi_i - \dot{e}_a \sin \psi_i \\ \frac{1}{r_i^g} (\dot{n}_a \sin \psi_i - \dot{e}_a \cos \psi_i) \end{bmatrix} \triangleq f_i(\mathbf{x}_i, \mathbf{u}_i), \end{aligned}$$

where

$$\mathbf{u}_i = [n_a \ e_a]^\top.$$

The Jacobian of the aircraft dynamics is given by

$$\frac{\partial f_a}{\partial \mathbf{x}_a}(\mathbf{x}, \mathbf{u}) = \begin{bmatrix} \mathbf{0}_{3 \times 3} & \mathbf{I}_{3 \times 3} & \mathbf{0}_{3 \times 3} \\ \mathbf{0}_{3 \times 3} & \mathbf{0}_{3 \times 3} & \frac{\partial R_i^b(\Theta) \mathbf{a}^b}{\partial \Theta} \\ \mathbf{0}_{3 \times 3} & \mathbf{0}_{3 \times 3} & \frac{\partial S(\Theta) \boldsymbol{\omega}}{\partial \Theta} \end{bmatrix}, \quad (5)$$

where

$$\begin{aligned} &\frac{\partial R_i^b(\Theta) \mathbf{a}^b}{\partial \Theta} \\ &= a_x \begin{bmatrix} 0 & -s_\theta c_\psi & -c_\theta s_\psi \\ 0 & -s_\theta s_\psi & c_\theta c_\psi \\ 0 & -c_\theta & 0 \end{bmatrix} \\ &+ a_y \begin{bmatrix} c_\phi s_\theta c_\psi + s_\phi s_\psi & s_\phi c_\theta c_\psi & -s_\phi s_\theta s_\psi - c_\phi c_\psi \\ c_\phi s_\theta s_\psi - s_\phi c_\psi & s_\phi c_\theta s_\psi & s_\phi s_\theta c_\psi - c_\phi s_\psi \\ c_\phi c_\theta & -s_\phi s_\theta & 0 \end{bmatrix} \\ &+ a_y \begin{bmatrix} -s_\phi s_\theta c_\psi + c_\phi s_\psi & c_\phi c_\theta c_\psi & -c_\phi s_\theta s_\psi + s_\phi c_\psi \\ -s_\phi s_\theta s_\psi - c_\phi c_\psi & c_\phi c_\theta s_\psi & c_\phi s_\theta c_\psi + s_\phi s_\psi \\ -s_\phi c_\theta & -c_\phi s_\theta & 0 \end{bmatrix}, \end{aligned}$$

and

$$\frac{\partial S(\Theta) \boldsymbol{\omega}}{\partial \Theta} = \begin{bmatrix} qc_\phi t_\theta - rs_\phi t_\theta & q \frac{s_\phi}{c_\theta^2} + r \frac{c_\phi}{c_\theta^2} & 0 \\ -qs_\phi - rc_\phi & 0 & 0 \\ q \frac{c_\phi}{c_\theta} - r \frac{s_\phi}{c_\theta} & q \frac{s_\phi s_\theta}{c_\theta^2} + r \frac{c_\phi s_\theta}{c_\theta^2} & 0 \end{bmatrix},$$

with $c_* \triangleq \cos(*)$, $s_* \triangleq \sin(*)$, and $t_* \triangleq \tan(*)$. Similarly, the Jacobians with respect to the input are given by

$$\frac{\partial}{\partial \mathbf{u}} f_a(\mathbf{x}, \mathbf{u}) = \begin{bmatrix} \mathbf{0}_{3 \times 3} & \mathbf{0}_{3 \times 3} \\ R_i^b(\Omega) & \mathbf{0}_{3 \times 3} \\ \mathbf{0}_{3 \times 3} & R_i^b(\Theta) \end{bmatrix}$$

and

$$\frac{\partial}{\partial \mathbf{u}} f_i(\mathbf{x}, \mathbf{u}) = \mathbf{0}_{2 \times 1}.$$

The Jacobian of the scatterer states with respect to the aircraft state is

$$\frac{\partial}{\partial \mathbf{x}_a} f_i(\mathbf{x}, \mathbf{u}) = \begin{bmatrix} \mathbf{0}_{1 \times 3} & -\cos \psi_i & \frac{\sin \psi_i}{r_i^g} & \mathbf{0}_{1 \times 4} \\ \mathbf{0}_{1 \times 3} & -\sin \psi_i & -\frac{\cos \psi_i}{r_i^g} & \mathbf{0}_{1 \times 4} \end{bmatrix},$$

and with respect to the scatterer state, the Jacobian is

$$\begin{aligned} &\frac{\partial}{\partial \mathbf{x}_i} f_i(\mathbf{x}, \mathbf{u}) \\ &= \begin{bmatrix} 0 & -\dot{n}_a \sin \psi_i - \dot{e}_a \cos \psi_i \\ \frac{1}{(r_i^g)^2} (-\dot{n}_a \sin \psi_i + \dot{e}_a \cos \psi_i) & \frac{\dot{n}_a \cos \psi_i + \dot{e}_a \sin \psi_i}{r_i^g} \end{bmatrix} \end{aligned}$$

when $i \neq j$, $\frac{\partial f_i}{\partial \mathbf{x}_j}(\mathbf{x}, \mathbf{u}) = \mathbf{0}_{2 \times 2n}$.

C. Update Sensor Dynamics

1) *GPS*: GPS measures

$$\mathbf{y}_{\text{GPS}} = [n_a \ e_a \ d_a \ V_g \ \chi]^\top,$$

where the ground velocity is defined as

$$V_g = \sqrt{\dot{n}_a^2 + \dot{e}_a^2}$$

and the heading is defined as

$$\chi = \text{atan} \left(\frac{\dot{n}_a}{\dot{e}_a} \right).$$

2) *Magnetometer*: Magnetometers measure the Earth's magnetic field in three dimensions, while we use a digital compass, which measures ψ , resulting in

$$y_{\text{mag}} = \psi.$$

Using a magnetometer allows for a consistent bearing measurement to be present throughout the flight.

3) *Coordinated Turn Pseudomeasurement*: The standard coordinated turn condition

$$\dot{\psi} = \frac{g}{V} \tan \psi$$

is imposed to make the roll angle observable. From (4), the turn condition becomes

$$\dot{\psi} = \frac{\sin \phi}{\cos \theta} q + \frac{\cos \phi}{\cos \theta} r.$$

Accordingly, the coordinated turn pseudomeasurement (which should nominally be zero) is

$$y_{\text{turn}} = \frac{\sin \phi}{\cos \theta} q + \frac{\cos \phi}{\cos \theta} r - \frac{g}{\sqrt{\dot{n}_a^2 + \dot{e}_a^2}} \tan \phi.$$

4) *AGL*: Using nadir, the AGL measurement is defined as

$$y_{\text{AGL}} = -d.$$

5) *Scatterer Range Measurement*: The range to each scatterer is modeled as

$$\begin{aligned} r_i &= \sqrt{(n_i - n_a)^2 + (e_i - e_a)^2 + d_a^2} \\ &= \sqrt{(r_i^g)^2 + d_a^2} \end{aligned} \quad (6)$$

with the resulting range measurements given by

$$y_r = [r_1 \quad \dots \quad r_N]^\top.$$

6) *Relative Range Pseudomeasurement*: While the relative positioning of each scatter is arbitrary, the relative range is measured when scatterers are both measured during the same chirp. This may be represented as

$$r_{ij} = r_i - r_j,$$

with the resulting relative range measurements given by

$$y_\Delta = [r_{12} \quad \dots \quad r_{(N-1)N}]^\top.$$

7) *Measurement Model*: The resulting measurement model is given by

$$y_k = h(\mathbf{x}_k) + \eta_k,$$

where

$$h(\mathbf{x}) = [h_{\text{GPS}} \quad h_{\text{mag}} \quad h_{\text{turn}} \quad h_{\text{AGL}} \quad h_r \quad h_\Delta]^\top$$

and η_k is the measurement noise.

The corresponding Jacobian is

$$\frac{\partial h}{\partial \mathbf{x}} = \begin{bmatrix} \frac{\partial h_{\text{GPS}}}{\partial \mathbf{x}_a} & \frac{\partial h_{\text{GPS}}}{\partial \mathbf{x}_s} \\ \frac{\partial h_{\text{mag}}}{\partial \mathbf{x}_a} & \frac{\partial h_{\text{mag}}}{\partial \mathbf{x}_s} \\ \frac{\partial h_{\text{turn}}}{\partial \mathbf{x}_a} & \frac{\partial h_{\text{turn}}}{\partial \mathbf{x}_s} \\ \frac{\partial h_{\text{AGL}}}{\partial \mathbf{x}_a} & \frac{\partial h_{\text{AGL}}}{\partial \mathbf{x}_s} \\ \frac{\partial h_r}{\partial \mathbf{x}_a} & \frac{\partial h_r}{\partial \mathbf{x}_s} \\ \frac{\partial h_\Delta}{\partial \mathbf{x}_a} & \frac{\partial h_\Delta}{\partial \mathbf{x}_r} \end{bmatrix}.$$

The Jacobian, with respect to the aircraft state \mathbf{x}_a , for the nonscatterer state terms are

$$\frac{\partial h_{\text{GPS}}}{\partial \mathbf{x}_a} = \begin{bmatrix} 1 & 0 & 0 & 0 & 0 & 0 & 0 & 0 & 0 \\ 0 & 1 & 0 & 0 & 0 & 0 & 0 & 0 & 0 \\ 0 & 0 & -1 & 0 & 0 & 0 & 0 & 0 & 0 \\ 0 & 0 & 0 & \frac{\dot{n}_a}{V_g} & \frac{\dot{e}_a}{V_g} & 0 & 0 & 0 & 0 \\ 0 & 0 & 0 & -\frac{1}{V_g^2} & -\frac{\dot{n}_a}{V_g^2} & 0 & 0 & 0 & 0 \end{bmatrix},$$

$$\frac{\partial h_{\text{mag}}}{\partial \mathbf{x}_a} = [0 \quad 0 \quad 0 \quad 0 \quad 0 \quad 0 \quad 0 \quad 0 \quad 1],$$

$$\frac{\partial h_{\text{turn}}}{\partial \mathbf{x}_a} = \begin{bmatrix} 0 \\ 0 \\ 0 \\ H_1(\mathbf{x}) \\ H_2(\mathbf{x}) \\ 0 \\ H_3(\mathbf{x}) \\ H_4(\mathbf{x}) \\ 0 \end{bmatrix}^\top,$$

$$\frac{\partial h_{\text{AGL}}}{\partial \mathbf{x}_a} = [0 \quad 0 \quad -1 \quad 0 \quad 0 \quad 0 \quad 0 \quad 0 \quad 0],$$

where

$$H_1(\mathbf{x}) = \frac{g \dot{n}_a \tan \phi}{V_g^3},$$

$$H_2(\mathbf{x}) = \frac{g \dot{e}_a \tan \phi}{V_g^3},$$

$$H_3(\mathbf{x}) = \frac{\cos \phi}{\cos \theta} q - \frac{\sin \phi}{\cos \theta} r - \frac{g \sec^2 \phi}{V_g},$$

$$H_4(\mathbf{x}) = \left(\frac{\sin \phi}{\cos \theta} q + \frac{\cos \phi}{\cos \theta} r \right) \tan \theta.$$

The Jacobians of the nonscatterer measurements with respect to any given scatterer state, \mathbf{x}_i , are all zero.

Calculating the partial derivative of the scatterer i for range measurement h_r with respect to the aircraft state gives

$$\frac{\partial}{\partial \mathbf{x}_a} h_{r,i}(\mathbf{x}) = \begin{bmatrix} 0 & 0 & \frac{h_a}{r_i} & 0 & 0 & 0 & 0 & 0 & 0 \end{bmatrix},$$

and calculating the partial derivative of h_r with respect to the scatterer state gives

$$\frac{\partial}{\partial \mathbf{x}_i} h_i(\mathbf{x}) = \begin{bmatrix} \frac{r_i^g}{r_i} & 0 \end{bmatrix}.$$

The partial derivative of the relative scatterer range measurement h_{Δ} with respect to the state is

$$\frac{\partial}{\partial \mathbf{x}_a} h_{ij}(\mathbf{x}) = \begin{bmatrix} 0 \\ 0 \\ \frac{h_a}{r_i} - \frac{h_a}{r_j} \\ 0 \\ 0 \\ 0 \\ 0 \\ 0 \end{bmatrix}^T,$$

$$\frac{\partial}{\partial \mathbf{x}_i} h_{ij}(\mathbf{x}) = \begin{bmatrix} \frac{r_j^g}{r_i} & 0 \end{bmatrix},$$

and

$$\frac{\partial}{\partial \mathbf{x}_j} h_{ij}(\mathbf{x}) = \begin{bmatrix} -\frac{r_j^g}{r_j} & 0 \end{bmatrix},$$

with

$$\frac{\partial}{\partial \mathbf{x}_m} h_{ij}(\mathbf{x}) = \mathbf{0}_{1 \times 2},$$

where $m \neq i$ and $m \neq j$.

8) *Range Rate*: While the R-RANSAC algorithm performs a polynomial fit to the range progression, it also estimates the range rate \dot{r}_i to each scatterer. The range rate may be calculated as

$$\dot{r}_i = \dot{n}_a \cos \psi_i \cos \phi_i + \dot{e}_a \sin \psi_i \cos \phi_i + \dot{d}_a \sin \phi_i. \quad (7)$$

By defining

$$\begin{bmatrix} \dot{n}_a \\ \dot{e}_a \end{bmatrix} = \begin{bmatrix} V_g \cos \psi_a \\ V_g \sin \psi_a \end{bmatrix}$$

and

$$V_g = \sqrt{\dot{n}_a^2 + \dot{e}_a^2},$$

the range rate equation may be written as

$$\frac{\dot{r}_i - \dot{d}_a \sin \phi_i}{\cos \phi_i} = V_g \cos \psi_a \cos \psi_i + V_g \sin \psi_a \sin \psi_i$$

$$= V_g \cos(\psi_i - \psi_a),$$

resulting in

$$\psi_i = \arccos \left(\frac{\dot{r}_i - \dot{d}_a \sin \phi_i}{\cos \phi_i \sqrt{\dot{n}_a^2 + \dot{e}_a^2}} \right) + \psi_a,$$

which, using (2) and the flat-Earth assumption, may be calculated as

$$\psi_i = \arccos \left(\frac{\dot{r}_i r_i + \dot{d}_a d_a}{\sqrt{r_i^2 - h_a^2} \sqrt{\dot{n}_a^2 + \dot{e}_a^2}} \right) + \psi_a. \quad (8)$$

This allows for the azimuth angle to be estimated from the scatterer state and range rate. Note that the result may be infinite, but this occurs only when $V_g = 0$ (i.e., the aircraft has no ground velocity) or when $\phi_i = 0$ (i.e., the aircraft is at the same elevation as the scatterer).

D. New Scatterer State Initialization

For SAR systems, the typical antenna beam width and aircraft speeds often results in point scatterers being illuminated for only a few seconds (as shown in Fig. 2). During this small time window, it is necessary to identify, track, and estimate the position of the scatterer with sufficient accuracy to estimate small variations in the aircraft's position. Accordingly, an increased accuracy in each scatterer's initial position greatly improves the estimates of the aircraft's position. For this reason, a range rate pseudomeasurement is used to provide an initial azimuth angle measurement.

When a new scatterer i is first identified, at time t_k , its state is initialized as

$$\mathbf{x}_i[t_k^+] = [r_i^g[t_k^+] \ \psi_i[t_k^+]]^T,$$

where $r_i^g[t_k^+]$ is the ground range estimate calculated as

$$r_i^g[t_k^+] = \sqrt{r_i^2[t_k] - d_a^2[t_k]},$$

and $\psi_i[t_k^+]$ is the azimuth angle pseudomeasurement calculated as

$$\psi_i[t_k^+] = \psi_a[t_k^-] + \arccos \left(\frac{\dot{r}_i[t_k] r_i[t_k] + \dot{d}_a[t_k^-] d_a[t_k^-]}{\sqrt{r_i^2[t_k] - d_a^2[t_k^-]} \sqrt{\dot{n}_a^2[t_k^-] + \dot{e}_a^2[t_k^-]}} \right),$$

where $r_i[t_k]$ is the R-RANSAC measurement, $\dot{r}_i[t_k]$ is the R-RANSAC pseudomeasurement, and $d_a[t_k^-]$, $\dot{n}_a[t_k^-]$, $\dot{e}_a[t_k^-]$, $\dot{d}_a[t_k^-]$, and $y_a[t_k^-]$ are current aircraft state estimates.

Additionally, the new scatterer EKF covariance terms must be updated. The new covariance terms are set to

$$\text{cov}[\mathbf{x}_i^* \mathbf{x}_i^{*T}] = \begin{bmatrix} \sigma_r & 0 \\ 0 & \sigma_\phi \end{bmatrix},$$

where the range and elevation angle standard deviation are σ_r^2 and σ_ϕ^2 , respectively, and

$$\text{cov}[\mathbf{x}_a^* \mathbf{x}_i^{*T}] = \mathbf{0}_{9 \times 2}.$$

The scatterer covariance terms, when $i \neq j$, are set to

$$\text{cov}[\mathbf{x}_i^* \mathbf{x}_j^{*T}] = \mathbf{0}_{2 \times 2}.$$

IV. RESULTS

As mentioned in section II-B4, a variety of association and tracking errors can and do occur. Accordingly, a simulation was run to demonstrate the accuracy of our approach where no data association errors occur. Fig. 7 shows the average, best, and worst results from the 10 Monte Carlo simulations from section III-D when integrated with an EKF and a navigation-grade IMU. During the simulation, the aircraft navigated for 60 s, moving approximately 2.7 km. The unknown point scatterers were positioned on a periodic grid. The IMU drift is approximately 260 m (or 9.6% drift rate), while the average drift error of the EKF was approximately 2 m

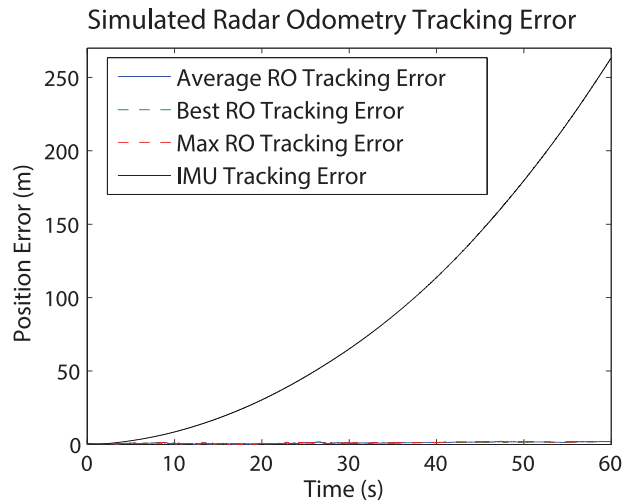


Fig. 7. Radar odometry–simulated flight error. The solid black line indicates the drift error with the navigation-grade IMU alone, while the blue line indicates the average of 10 Monte Carlo results. The best and worst results are shown in red and green, respectively.

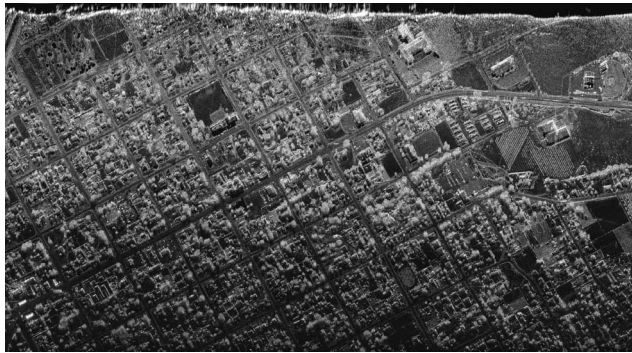


Fig. 8. Processed image formed from real flight data.

(0.076% drift), with a worst-case drift rate of 2.2 m (or .076% drift) and a best-case drift of 1.96 m (or 0.073% drift).

The real flight tests were performed using an SAR mounted to a Cessna aircraft. A SAR image formed from the flight data is shown in Fig. 8. The elevation rises approximately 50 m during the course of the flight. As the algorithm assumes a flat-Earth model, an elevation-compensated GPS was used as truth data for the results. From the start to the end of the flight track, there is also a 7- to 29-m elevation drop in the cross-track direction. In addition to the violated flat-terrain assumption, many point scatterers from features found in trees and on buildings may be positioned significantly higher than ground level. As we were provided with the test data, all results are post-processed, though the computational complexity of the algorithm allows for real-time implementation on modest hardware.

During the flight, the readings from a navigation-grade IMU were recorded. The IMU's gyro has a 1-sigma standard deviation of 1 deg/h, while its accelerometer standard deviation is 0.0003 g, more precise than those found on small UAVs. The test involves initially using the

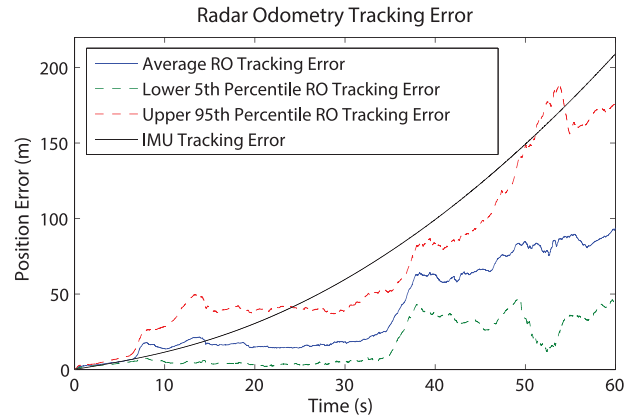


Fig. 9. Radar odometry real flight error. The solid black line indicates the drift error with the navigation-grade IMU alone, while the blue line indicates the average of 100 Monte Carlo results. The upper 95th-percentile error and the lower 5th-percentile error results are shown in red and green, respectively.

elevation-compensated GPS, during which time the algorithm estimates the point scatterer locations. After 16 s of flight (approximately 560 m in the along-track direction), the GPS signal was lost, and the test continued for 60 s (around 2.4 km). A simulated consumer-grade magnetometer, with a sigma of 0.3 deg, is used as a bearing measurement.

Fig. 9 shows the results of the radar odometry position estimation error after GPS signal is lost. As can be seen, the data association errors, due to the extremely cluttered environment, degraded the results during the first 20 s of the radar collect. As the flight continued, however, proper association and tracking resulted in improved results, though a single flight track improperly deviated for the time between 48 and 54 s. Throughout the flight, many clutter and noise sources are improperly identified and tracked, though, as a whole, the R-RANSAC tracking approach demonstrated a significant improvement in the results. The unaided IMU drifts 209 m (or approximately a 9.1% drift rate), while the average radar odometry drift rate is 92 m (3.4% drift rate). While the 95th-percentile worst-case drift was 175 m (7.3%), the 5th-percentile drift was 42 m (1.8% drift rate). With a commercial-grade IMU, even better improvements are expected.

V. CONCLUSION

When GPS is lost or denied, accurate navigation of current UAVs is subject to the IMU's drift rates. We have demonstrated that in real, cluttered environments, R-RANSAC is able to make use of arbitrary point scatterers to improve the navigation of an unaided IMU. Additionally, we have shown that the radar odometry algorithm developed in this paper is able to improve the real flight drift error 3.4% on average, as compared to 9.1% when using an unaided navigation-grade IMU. Our results indicate that radar odometry is a feasible and robust solution for navigating in unknown, GPS-denied environments. Additionally, radar allows for all-weather, all-time-of-day navigation with no degradation of results.

Future work involves further improving the radar odometry results, specifically improving the clutter suppression, improving the AGL measurement, and assessing the systems observability.

ACKNOWLEDGMENT

This research was partially funded with government support through the Department of Defense, Air Force Office of Scientific Research, National Defense Science and Engineering Graduate (NDSEG) Fellowship, 32 CFR 168a.

REFERENCES

- [1] Caballero, F., Merino, L., Ferruz, J., and Ollero, A. Vision-based odometry and SLAM for medium and high altitude flying UAVs. *Journal of Intelligent and Robotic Systems*, **54**, 1–3 (Jul. 2008), 137–161.
- [2] Fraundorfer, F., and Scaramuzza, D. Visual odometry: part II: matching, robustness, optimization, and applications. *Robotics & Automation Magazine*, **19**, 2 (2012), 78–90.
- [3] Konolige, K., Agrawal, M., and Sola, J. Large-scale visual odometry for rough terrain. In *Robotics Research*, Heidelberg, Germany: Springer Berlin Heidelberg (2010), 201–212.
- [4] Konolige, K., Bowman, J., Chen, J., Mihelich, P., Calonder, M., Lepetit, V., and Fua, P. View-based maps. *International Journal of Robotics Research*, **29**, 8 (2010), 941.
- [5] Nistér, D. An efficient solution to the five-point relative pose problem. *IEEE Transactions on Pattern Analysis and Machine Intelligence*, **26**, 6 (2004), 756–770.
- [6] Scaramuzza, D., and Fraundorfer, F. Visual odometry: part I: the first 30 years and fundamentals. *Robotics & Automation Magazine*, **18**, 4 (Dec. 2011), 80–92.
- [7] Ahmad, A., Huang, S., Wang, J. J., and Dissanayake, M. G. A new state vector for range-only SLAM. In *2011 Chinese Control and Decision Conference*, Mianyang, China, May 2011, 3404–3409.
- [8] Durrant-Whyte, H. F., Bell, E., and Avery, P. The design of a radar-based navigation system for large outdoor vehicles. *Proceedings of 1995 IEEE International Conference on Robotics and Automation*, **1** (1995), 764–769.
- [9] Leonard, J. J., and Durrant-Whyte, H. F. Simultaneous map building and localization for an autonomous mobile robot. In *IEEE/RSJ International Workshop on Intelligent Robots and Systems 91. Intelligence for Mechanical Systems, Proceedings IROS '91*, Osaka, Japan, November 1991, 1442–1447.
- [10] Schneider, A. Observability of relative navigation using range-only measurements. *IEEE Transactions on Aerospace and Electronic Systems*, **21**, 4 (Jul. 1985), 569–581.
- [11] Hagen, O. K., Anonsen, K. B., and Saebo, T. O. Low altitude AUV terrain navigation using an interferometric sidescan sonar. In *OCEANS 2011*, Waikoloa, HI, September 2011.
- [12] Newman, P. M., and Leonard, J. J. Pure range-only sub-sea SLAM. In *Proceedings of the International Conference on Robotics and Automation, ICRA '03*, **2** (2003), 1921–1926.
- [13] Marco, D., and Healey, A. Local area navigation using sonar feature extraction and model based predictive control. *Proceedings of Symposium on Autonomous Underwater Vehicle Technology*, Monterey, CA, June 1996, 67–77.
- [14] Thrun, S., Burgard, W., and Fox, D. A probabilistic approach to concurrent mapping and localization for mobile robots. *Autonomous Robots*, **25** (1998), 1–25.
- [15] Smith, R. A. Radar navigation. *Electrical Engineers—Part IIIA*, **93**, 1 (1946), 331–342.
- [16] Kauffman, K. Fast target tracking technique for synthetic aperture radars. Master's thesis, Miami University, Oxford, OH, 2009.
- [17] Kauffman, K., Garmatyuk, D., and Morton, Y. T. J. Efficient sparse target tracking algorithm for navigation with UWB-OFDM radar sensors. In *Proceedings of the IEEE 2009 National Aerospace & Electronics Conference*, Jul. 2009, 14–17.
- [18] Kauffman, K., Morton, Y. T. J., Raquet, J., and Garmatyuk, D. Simulation study of UWB-OFDM SAR for dead-reckoning navigation. In *Proceedings of the 2010 International Technical Meeting of the Institute of Navigation*, January 25–27 2010, 153–160.
- [19] Kauffman, K., Raquet, J., Morton, Y. T. J., and Garmatyuk, D. Simulation study of UWB-OFDM SAR for navigation using an extended Kalman filter. In *ION GNSS*, Portland, OR, September 2010, 2443–2451.
- [20] Kauffman, K., and Raquet, J. Enhanced feature detection and tracking algorithm for UWB-OFDM SAR navigation. In *Proceedings of the 2011 IEEE National Aerospace and Electronics Conference*, Jul. 2011, 261–269.
- [21] Kauffman, K., Raquet, J., Morton, Y. T. J., and Garmatyuk, D. Simulation study of UWB-OFDM SAR for navigation with INS integration. In *Proceedings of the 2011 International Technical Meeting of the Institute of Navigation*, San Diego, CA, January 2011, 184–191.
- [22] Kauffman, K. Radar based navigation in unknown terrain. PhD dissertation, Air Force Institute of Technology, Wright-Patterson Air Force Base, OH, 2012.
- [23] Kauffman, K., Raquet, J., Morton, Y. T. J., and Garmatyuk, D. Experimental study of UWB-OFDM SAR for indoor navigation with INS integration. In *ION GNSS*, Nashville, TN, September 2012, 3847–3852.
- [24] Kauffman, K., Raquet, J., Morton, Y. T. J., and Garmatyuk, D. Real-time UWB-OFDM radar-based navigation in unknown terrain. *IEEE Transactions on Aerospace and Electronic Systems*, **49**, 3 (2013), 1453–1466.
- [25] Kim, J.-H., and Sukkarieh, S. Autonomous airborne navigation in unknown terrain environments. *IEEE Transactions on Aerospace and Electronic Systems*, **40**, 3 (2004), 1031–1045.
- [26] Garmatyuk, D., Schuerger, J., Kauffman, K., and Spalding, S. Wideband OFDM system for radar and communications. In *2009 IEEE Radar Conference*, Pasadena, CA, May 2009, 1–6.
- [27] Lundgreen, R. B., Thompson, D. G., Arnold, D. V., Long, D. G., and Miner, G. F.

- Initial results of a low-cost SAR: YINSAR.
IGARSS 2000. IEEE 2000 International Geoscience and Remote Sensing Symposium. Taking the Pulse of the Planet: The Role of Remote Sensing in Managing the Environment. Proceedings (Cat. No.00CH37120), 7 (2000), 3045–3047.
- [28] Schneider, D. (2009)
Winner: radio eye in the sky, IEEE Spectrum.
[Online]. Available: <http://spectrum.ieee.org/computing/hardware/winner-radio-eye-in-the-sky>.
- [29] Zaugg, E. C., Hudson, D. L., and Long, D. G.
The BYU SAR: a small, student-built SAR for UAV operation.
In *2006 IEEE International Symposium on Geoscience and Remote Sensing*, Denver, CO (Jul. 2006), 411–414.
- [30] Henley, A.
Terrain aided navigation: current status, techniques for flat terrain and reference data requirements.
In *Position Location and Navigation Symposium, Proceedings of the IEEE*, Las Vegas, NV (1990), 608–615.
- [31] Hostetler, L. D., and Andreas, R. D.
Nonlinear Kalman filtering techniques for terrain-aided navigation.
IEEE Transactions on Automatic Control, **28**, 3 (Mar. 1983), 315–323.
- [32] Nordlund, P.-J., and Gustafsson, F.
Marginalized particle filter for accurate and reliable terrain-aided navigation.
IEEE Transactions on Aerospace and Electronic Systems, **45**, 4 (2009), 1385–1399.
- [33] Langer, D.
An integrated MMW radar system for outdoor navigation.
Proceedings of the 1996 IEEE International Conference on Robotics and Automation, Minneapolis, MN, Vol 1, (Apr. 1996), 417–422.
- [34] Langer, D.
An integrated MMW radar system for outdoor navigation.
Ph.D. dissertation, Carnegie Mellon University, Pittsburgh, PA, 1997.
- [35] Deibler, T., and Thielecke, J.
Feature based indoor mapping using a bat-type UWB radar.
Ultra-Wideband, Proceedings of the 2009 IEEE International Conference on (ICUWB2009), **2009** (2009), 475–479.
- [36] Jose, E., and Adams, M. D.
An augmented state SLAM formulation for multiple line-of-sight features with millimeter wave RADAR.
2005 IEEE/RSJ International Conference on Intelligent Robots and Systems, Alberta, Canada, Aug. 2005, 3087–3092.
- [37] Marck, J. W., Mohamoud, A., Houwen, E., and Heijster, R. V.
Indoor radar SLAM A radar application for vision and GPS denied environments.
In *Radar Conference, Proceedings of the 10th European*, Nuremburg, Germany, Oct. 2013, 471–474.
- [38] de Haag, M. U., Vadlamani, A. K., Campbell, J. L., and Dickman, J.
Application of laser range scanner based terrain referenced navigation systems for aircraft guidance.
In *Proceedings of the Third IEEE International Workshop on Electronic Design, Test, and Applications*, Kuala Lumpur, Jan. 2006, 6–274.
- [39] Stahn, R., Heiserich, G., and Stopp, A.
Laser scanner-based navigation for commercial vehicles.
Intelligent Vehicles Symposium, Proceedings of the 2007 IEEE, **200** (2007), 969–974.
- [40] Toutin, T.
Comparison of stereo-extracted DTM from different high-resolution sensors: SPOT-5, EROS-A, IKONOS-II, and QuickBird.
IEEE Transactions on Geoscience and Remote Sensing, **42**, 10 (2004), 2121–2129.
- [41] Vadlamani, A. K., and de Haag, M. U.
Improved downward-looking terrain database integrity monitor and terrain navigation.
In *Aerospace Conference, 2004. Proceedings*, 2004, 1594–1607.
- [42] Vadlamani, A. K., and de Haag, M. U.
Flight test results of loose integration of dual airborne laser scanners (DALS)/INS.
In *2008 IEEE/ION Position, Location and Navigation Symposium*, Monterey, CA, May 2008, 304–311.
- [43] Schwartz, M.
A coincidence procedure for signal detection.
IEEE Transactions on Information Theory, **2**, 4 (Dec. 1956), 135–139.
- [44] Walker, J. F.
Performance data for a double-threshold detection radar.
IEEE Transactions on Aerospace and Electronic Systems, **7**, 1 (1971), 142–146.
- [45] Quist, E. B., and Beard, R. W.
Radar odometry on small unmanned aircraft.
In *AIAA Guidance, Navigation, and Control (GNC) Conference*, Boston, MA, August 2013, 1–18.
- [46] Quist, E. B., and Beard, R. W.
Radar odometry on fixed-wing small unmanned aircraft.
In *IEEE Transactions on Aerospace and Electronic Systems*, **52**, 1 (Feb. 2016), 396–410.
- [47] Niedfeldt, P. C., and Beard, R. W.
Recursive RANSAC: multiple signal estimation with outliers.
In *Proceedings of 9th IFAC Symposium on Nonlinear Control Systems (NOLCOS)*, **46**, 23 (2013), 430–435.
- [48] Niedfeldt, P. C.
Recursive-RANSAC: a novel algorithm for tracking multiple targets in clutter.
Ph.D. dissertation, Brigham Young University, Provo, UT, 2014.
- [49] Niedfeldt, P. C., Quist, E. B., and Beard, R. W.
Characterizing range progression of SAR point scatterers with recursive RANSAC.
In *IEEE Proceedings on Radar Conference*, Cincinnati, OH, May 2014, 712–717.
- [50] Fischler, M. A., and Bolles, R. C.
Random sample consensus: a paradigm for model fitting with applications to image analysis and automated cartography.
Communications of the ACM, **24**, 6 (1981), 381–395.
- [51] Bar-Shalom, Y., and Fortmann, T. E.
Tracking and Data Association. New York: Academic Press, 1988.
- [52] Lerro, D., and Bar-Shalom, Y.
Tracking with debiased consistent converted measurements versus EKF.
IEEE Transactions on Aerospace and Electronic Systems, **2**, 3 (1993), XXX–XXX.
- [53] Blackman, S. S., and Popoli, R.
Design and Analysis of Modern Tracking Systems. Norwood, MA: Artech House, 1999.
- [54] Fortmann, T. E., Bar-Shalom, Y., and Scheff, M.
Multi-target tracking using joint probabilistic data association.
In *19th IEEE Conference on Decision and Control Including the Symposium on Adaptive Processes*, Albuquerque, NM, December 1980, 807–812.
- [55] Kurien, T., Blitz, A., Washburn, R., and Willsky, A.
Optimal maneuver detection and estimation in multiobject tracking,
In *6th MIT/ONR Workshop on Command, Control, and Communication Systems*, Cambridge, MA, July 1983, 164–171.
- [56] Reid, D. B.
An algorithm for tracking multiple targets.

- IEEE Transactions on Automatic Control*, **24**, 6 (Dec. 1979), 843–854.
- [57] Mahler, R. P. S.
A theoretical foundation for the Stein-Winter “probability hypothesis density (PHD)” multitarget tracking approach. Lockheed Martin, Bethesda, MD, Tech. Rep., 2000.
- [58] Mahler, R. P. S.
Multitarget Bayes filtering via first-order multitarget moments.
IEEE Transactions on Aerospace and Electronic Systems, **39**, 4 (Oct. 2003), 1152–1178.
- [59] Bar-Shalom, Y., and Tse, E.
Tracking in a cluttered environment with probabilistic data association.
Automatica, **11** (1975), 451–460.
- [60] Kim, J. H., and Sukkarieh, S.
Recasting SLAM—towards improving efficiency and platform independency.
In *Robotics Research*. Berlin: Springer, 2005, 1–10.
- [61] Munguia, R., and Grau, A.
A practical method for implementing an attitude and heading reference system.
International Journal of Advanced Robotic Systems, **11** (2014), 1.
- [62] Qi, H., and Moore, J. B.
Direct Kalman filtering approach for GPS/INS integration.
IEEE Transactions on Aerospace and Electronic Systems, **38** (2002), 144–149.
- [63] Wendel, J., Schlaile, C., and Trommer, G. F.
Direct Kalman filtering of GPS/INS for aerospace applications.
Proceedings of the International Symposium on Kinematic Systems in Geodesy, Geomatics and Navigation (KIS2001), Banf, Canada, Jun. 2001.
- [64] Lewis, F. L.
Optimal Estimation: With an Introduction to Stochastic Control Theory. New York: Wiley, 1986.
- [65] Beard, R. W., and McLain, T. W.
Small Unmanned Aircraft: Theory and Practice. Princeton, NJ: Princeton University Press, 2012.



Eric B. Quist received his B.S. degree in electrical engineering from Brigham Young University, Provo, Utah, in 2004; M.S. degree in electrical engineering from the University of Southern California, Los Angeles, in 2010; and Ph.D. degree in electrical engineering in 2015, also from Brigham Young University. Since 2010, he has been with IMSAR, Springville, Utah, where he is working on algorithms and system development. His interests include radar system design, embedded system development, and signal processing.



Peter C. Niedfeldt is currently on the technical staff at MIT Lincoln Laboratory, Lexington, Massachusetts. He graduated from Brigham Young University, Provo, Utah, with his Ph.D. and B.S. degrees in electrical engineering in 2014 and 2009, respectively. Summer internships include experience at UTRC (2013), AFRL (2010), and Raytheon (2008). His current interests include multiple target tracking, Bayesian estimation and filtering, space control, guidance and navigation, and autonomous systems.



Randal W. Beard received his B.S. degree in electrical engineering from the University of Utah, Salt Lake City, in 1991; M.S. degree in electrical engineering in 1993; M.S. degree in mathematics in 1994; and Ph.D. in 1995. Since 1996, he has been with the Electrical and Computer Engineering Department at Brigham Young University, Provo, Utah, where he is currently a professor. In 1997 and 1998, he was a Summer Faculty Fellow at the Jet Propulsion Laboratory, California Institute of Technology, Pasadena. His primary research focus is in autonomous systems, unmanned air vehicles, and multiple vehicle coordination. He is a fellow of the IEEE and an associate fellow of the AIAA. He is a former associate editor for the *IEEE Transactions on Automatic Control*, the *Journal of Intelligent and Robotics Systems*, and the *IEEE Control Systems Magazine*.